



The impact of alloy chemistry on the formation of a silicon-rich subscale on two classes of ferritic steels

Paul D. Jablonski ^{a,*}, John S. Sears ^{a,b}

^a National Energy Technology Laboratory, United States Department of Energy, 1450 Queen Ave. SW, Albany, OR 97321, USA

^b URS Corporation, P.O. Box 1959, Albany, OR 97321, USA

HIGHLIGHTS

- ▶ Two classes of ferritic stainless steels are examined for SOFC interconnect use.
- ▶ Avoidance of silica subscale may require Si to be as low as possible, perhaps zero.
- ▶ The silica subscale that forms in alloy 441ss is different from that in 430ss.
- ▶ The silica subscale that forms in alloy 441ss is less detrimental to ASR.

ARTICLE INFO

Article history:

Received 22 September 2012

Received in revised form

12 November 2012

Accepted 16 November 2012

Available online 29 November 2012

Keywords:

SOFC

Interconnect

Oxidation

ASR

Silicon

Laves

ABSTRACT

Stainless steel type 441 (UNS S44100) is being considered for application as a Solid Oxide Fuel Cell (SOFC) interconnect material. It had been thought that Laves phase that forms in this alloy preferentially consumes the Si present in the alloy microstructure, thereby avoiding formation of a Si-rich layer at the scale/metal interface. Recent work has shown this is not the case and a Si-rich layer does indeed form at the scale/metal interface. However, this layer is significantly different from the layer that forms in other ferritic stainless steels, for example, type 430. In this present work the Si-rich layer that forms on 441ss is examined and compared to the layer that forms on several 430-type alloys with varying low levels of Si. This research has shown that even at very low levels of Si (170 ppm), a Si-rich layer begins to form on the 430-type stainless steels. However, the morphology, particularly with respect to the thickness and continuity of the Si-rich subscale that forms in alloy 441ss, is modified in comparison to non-Laves forming ferritic stainless steels and therefore, may not be as detrimental to long term SOFC performance.

Published by Elsevier B.V.

1. Background and introduction

Technologies that increase energy efficiency are becoming increasingly important as they have the dual advantages of lower fuel consumption and reduced pollution (including CO₂) for a given energy output. Solid Oxide Fuel Cells (SOFC) are energy conversion devices that transform fuel to electrical energy in the absence of combustion. They have the potential for high efficiencies, especially when combined into an integrated fuel utilization system [1–4]. A significant advance was made with the development of cell components that could operate in a temperature range of 700–800 °C compared to previous systems which operated typically at

>1000 °C [5–10]. With temperature reduction metallic components for use as interconnects became possible. Metal interconnects have the advantage of being less costly to produce and they are more easily manufactured in comparison to their ceramic counterparts. Within a planar SOFC, an interconnect joins repeat units of the anode/electrolyte/cathode assembly so that useful levels of current and voltage can be obtained. In doing this the interconnect separates the fuel and air, and also becomes part of the electrical circuit. Even at elevated operating temperatures, candidate metallic interconnect alloys have low electrical resistivity compared to their ceramic counterparts.

Unfortunately, the candidate metal interconnects oxidize under both the anodic and cathodic conditions present within an SOFC. Thus a chief requirement for a metal interconnect is that the base metal oxide scale must be electrically conductive. Common high temperature alloys form oxide scales that contain Cr, Si, and Al oxides, among others. Under SOFC operating conditions chromia is

* Corresponding author. Tel.: +541 967 5982, 541 231 5210.

E-mail addresses: paul.jablonski@netl.doe.gov (P.D. Jablonski), john.sears@contr.netl.doe.gov (J.S. Sears).

an intrinsic semiconductor while both silica and alumina are strong insulators. Therefore, alloys that preferentially form chromia-based oxide scales are desirable for SOFC interconnects.

Many SOFC designs will need to operate at temperatures exceeding 700 °C. At these temperatures, in the moist SOFC cathode environment, Cr containing species evaporate and the Cr from these compounds deposits on electrochemically active sites at the cathode-electrolyte interface. This process degrades the electrical performance of the SOFC because the presence of Cr poisons the necessary electrochemical reactions that take place in the cathode [11–17]. However, the formation of a Cr–Mn spinel outer layer on top of a chromia subscale will reduce, but not eliminate, Cr evaporation. Thus, an oxide architecture of this nature will not prevent the Cr from poisoning the electrochemical reactions but it may delay it. Consequently, there has been considerable attention placed on developing coatings to prevent Cr migration from the stainless steel interconnects into the cathode [17–21].

Several commercial alloys have been developed for SOFC interconnect applications. These include Crofer 22 APU (ThyssenKrupp VDM), Hitachi ZMG 232 (Hitachi Metals), and Ebrite (Allegheny Ludlum), all of which form chromium-rich oxide scales under oxidizing conditions. One disadvantage of these alloys is that they are considered “specialty” alloys, due to the addition of rare earth elements and/or extra processing steps to lower Al and Si contents. As such this increases alloy cost and they are not as readily available as other ferritic stainless steels. Additionally, it has been observed that even with special processing, these alloys often contain sufficient Si to form at least a semi-continuous Si-rich subscale [22]. Several authors [23–25] have reported that 441ss can be utilized as an interconnect with good results, even though this alloy may contain up to 1 weight percent (wt%) Si [26] and yet remain within the 441ss nominal chemistry specification. Besides the usual Cr and Mn, 441ss also contains Nb and Ti and is known to form a Fe₂Nb-based Laves phase, an intermetallic with a C14 hexagonal crystal structure [27,28]. Previous research has shown that Si preferentially partitions to this phase over the ferritic matrix [25,29–32]. The Laves phase has also been observed to reside on ferritic grain boundaries [25,31–33], potentially serving as a blocking agent for grain boundary diffusion [34]. More recently, Jablonski et al. [32] showed that a Si-rich phase forms at the base of the oxide scale in alloy 441ss, disputing the effectiveness of Laves phase in either scavenging Si from the matrix or blocking diffusion. It further questions the long term viability of 441ss in interconnect applications.

The research performed herein was intended to definitively evaluate the Si-rich subscale that forms on 441ss in comparison to that which forms on comparable stainless steels such as 430ss. Furthermore, this work intends to establish the threshold level of Si above which a layer of resistive scale is expected to form.

2. Experimental

2.1. Alloy manufacture

High purity starting materials were used to formulate 441ss as per nominal chemistry and three heats of 430ss were made with varying low levels of Si (Table 1). Approximately 6800 g of high purity raw materials were formed into compacts prior to melting. Each alloy was induction melted under argon and poured into a 75 mm diameter cylindrical graphite mold with a zircon-based face coat to minimize carbon pickup. After casting, the hot-tops of each ingot were removed and a 2 mm thick slice was sectioned from each ingot for chemical analysis. The metal chemistries were determined by X-ray Fluorescence (XRF) using a Rigaku ZX Primus II, with NIST traceable standards (reported values are accurate to

Table 1

Experimental alloy measured chemistries are given in the table below in weight percent (wt%). The metal chemistries were determined by XRF with a Rigaku ZX Primus II utilizing NIST traceable standards (reported values are accurate to 0.01 wt %); carbon chemistries were determined with a LECO CS444LS using NIST certified standards (reported values are accurate to 0.002 wt%). The silicon in 430-E was determined by GDMS.

| Designation | Fe | C | Cr | Mn | Nb | Si | Ti |
|-------------|-----|-------|------|------|-----|-------|------|
| 441ss | Bal | 0.01 | 18.1 | 0.34 | 0.5 | 0.33 | 0.22 |
| 430-E | Bal | 0.005 | 17.0 | 0.38 | 0.0 | 0.017 | 0.0 |
| 430-F | Bal | 0.001 | 17.0 | 0.40 | 0.0 | 0.024 | 0.0 |
| 430-G | Bal | 0.001 | 17.3 | 0.45 | 0.0 | 0.050 | 0.0 |

0.01 wt%). Carbon chemistries were determined with a LECO CS444LS using NIST certified standards (reported values are accurate to 0.002 wt%). At the lowest levels, Si was determined by Glow Discharge Mass Spectrometry (GDMS). The sidewalls of the ingots were conditioned on a lathe, and each ingot was given a computationally optimized homogenization heat treatment [35]. The homogenized ingots were bagged in protective stainless steel foil pouches and preheated at 900 °C for 3 h to provide through-heating prior to fabrication. Hot working consisted of forging and rolling to fabricate the round ingots into slab shapes, which were ultimately formed into strip. The strips were hot worked to a thickness of approximately 3 mm. Subsequently, these strips were conditioned to remove oxidation products and other residual surface defects prior to cold rolling. Each alloy was then cold rolled to approximately 1 mm thickness.

2.2. Alloy testing and evaluation

Oxidation test coupons approximately 12 mm × 24 mm × sheet thickness were cut from the cold worked strip of each alloy. The coupons were polished to a 600 grit surface finish before exposure to laboratory air at 800 °C for 2000 h. Oxidized coupons were sectioned and polished via conventional metallographic procedures in order to view the scales in a cross-sectional orientation. Care was taken to avoid induced surface Si contamination from silica polishing media by only using submicron alumina or diamond for the final polishing steps. The cross-sections of each exposed alloy were analyzed by Scanning Electron Microscopy (SEM) using Energy Dispersive and Wavelength Dispersive X-ray Analysis (EDX and WDX) with in-situ standards for metal and oxide scale chemistry.

Selected samples were prepared for Transmission Electron Microscopy (TEM) examination using the Helios Nano Lab Dual Beam-Focused Ion Beam (DB-FIB) system. Specifically, this allowed sample preparation within the critical alloy/oxide scale region. The samples were then examined in a Philips/FEI CM200 TEM. The chemistries of select areas of interest were determined by EDX in the TEM.

3. Results

3.1. Chemistry

The alloy chemistries for the materials fabricated in this study are found in Table 1. Alloy 441ss has slightly higher Cr than the 430ss alloys (~18 vs. ~17 wt%) and similar Mn contents, ~0.4. It is noteworthy that alloy 441ss contains both Nb and Ti. The addition of these elements scavenges C and N in the alloy thereby stabilizing the ferrite phase. Alloy 430ss contains no Nb or Ti, and these alloys will form some austenite but only at temperatures much above the 800 °C exposure temperature of the present experiments. The other

significant difference between the 441ss and the experimental 430ss alloys is the level of Si. Both alloys in commercial form can contain up to 1 wt% Si. The 441ss alloy contains 0.33 wt% Si while the experimental 430ss alloys contain 170, 240 and 500 ppm Si (alloys E, F, and G, respectively). Note that these alloys are within the commercial specification for Si, which is less than 1 wt%.

3.2. Microstructure

3.2.1. SEM cross-sections

The SEM based WDX analysis of the three 430ss alloys well away from the oxide scale resulted in 0.08, 0.08 and 0.17 atomic percent (at%) Si (or 400, 400 and 900 ppm by weight) for alloys E, F, and G, respectively. These values are below what is generally accepted as the detection limit in SEM based WDX analysis and while these results differ from the higher precision bulk analysis, they showed that alloy 430-G had the highest Si level, and suggested a detection limit of about 0.1 wt% (1000 ppm). The back-scattered electron (BSE) detector was employed for all SEM imaging. Fig. 1 shows a typical cross-section of the 430-E alloy (170 ppm Si) after oxidation. The thin outer scale appeared slightly lighter (higher average atomic number) and contained both Cr and Mn while the thicker inner scale contained mainly Cr. A total of nine areas at the scale/metal interface were analyzed. The resulting Si content ranged from 0.2 to 0.4 at% (1000–3000 ppm by weight) while the analysis of the base metal 20–30 μm beneath the scale resulted in 0.07–0.09 at% Si (360–480 ppm by weight), suggesting a 3–6 fold increase in Si at the scale/metal interface. Fig. 2 shows a typical cross-section of the 430-F alloy (240 ppm Si) after oxidation. The majority of the scale on the 430-F alloy appeared similar to the 430-E alloy with a thin Cr–Mn outer scale on top of a Cr-rich scale. The Cr-rich scale constituted the bulk of the oxide. Some dark contrasting phases were observed at the scale/metal interface suggesting the presence of a low atomic number material. Analysis of eight areas along this interface resulted in Si values ranging from 0.1 to 0.3 at% Si (900–1800 ppm by weight). Analysis of the base metal 20–30 μm beneath the scale resulted in 0.07–0.09 at% Si (380–440 ppm by weight) – again suggesting an increase in Si at the scale/metal interface. Fig. 3 shows a typical cross-section of the 430-G alloy (500 ppm Si) after oxidation. Besides the thin Cr–Mn outer scale and thicker Cr-rich inner scale observed on the two alloys discussed previously, a nearly continuous dark phase was observed to appear at the scale/metal interface of alloy 430-G. Several examples of this region were analyzed resulting in 21–25 at%

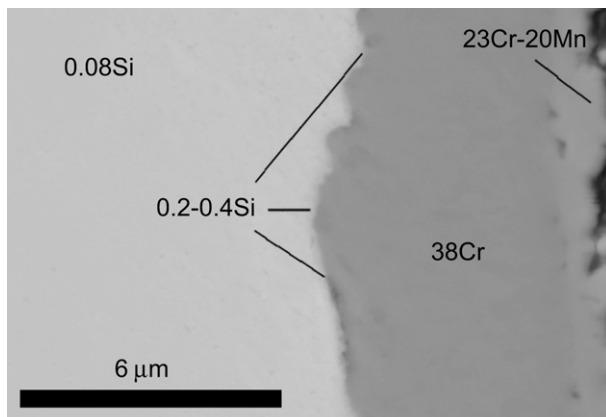


Fig. 1. SEM cross-section at the base metal/scale interface for alloy 430-E exposed for 2000 h at 800 °C is shown above. Note that the values are given in atomic percent (at%) and the balance is oxygen in the two outer scale layers (at right).

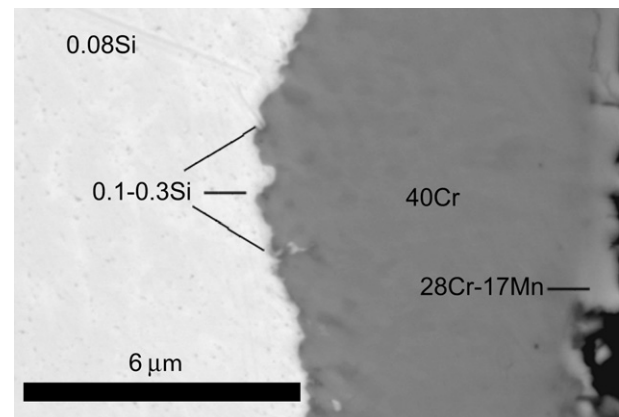


Fig. 2. SEM cross-section at the base metal/scale interface for alloy 430-F exposed for 2000 h at 800 °C is shown above. Note that the values are given in at% and the balance is oxygen in the two outer scale layers (at right).

% Si in the dark phase and 0.6–3.6 at% Si in regions of the scale/metal interface absent of this darker phase.

Fig. 4 shows a typical cross-section of the 441ss alloy after oxidation (first published in Ref. [32]). This alloy contains a thin outer Cr–Mn containing scale on top of a Cr-rich scale, which again constituted the bulk of the oxide. However, since this alloy also contained Nb and Ti, Laves phase was observed in the matrix (bright equiaxed particles) as well as internal oxidation of Ti below the scale/metal interface. The Si content in the matrix analyzed at 0.32 wt% about 10 μm beneath the scale (i.e., in good agreement with the bulk analysis). As reported previously [32], substantial Si was detected at the scale/metal interface, similar to that found in alloy 430-G (about 21 at%).

3.2.2. TEM cross-sections

Several FIB cross-sections containing oxide scale from each of the alloys were examined after 2000 h exposure at 800 °C. The fundamental features of the oxide scales grown on each of the alloys are very similar: An external columnar region of Cr–Mn spinel oxide grown on top of thicker equiaxed grained, nearly pure Cr oxide scale (Fig. 5). Visible in the image is a protective Pt layer on top of the outer Cr–Mn spinel and also the Si-rich subscale.

Fig. 6 details the morphology and crystal structure of the outer spinel grains on the 441ss. The 441ss spinel contained 60–65 at% Cr

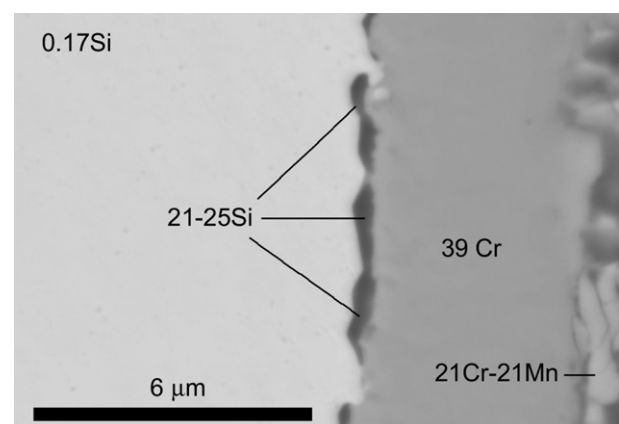


Fig. 3. SEM cross-section at the base metal/scale interface for alloy 430-G exposed for 2000 h at 800 °C is shown above. Note that the values are given in at% and the balance is oxygen with the exception of the matrix Si level (upper left).

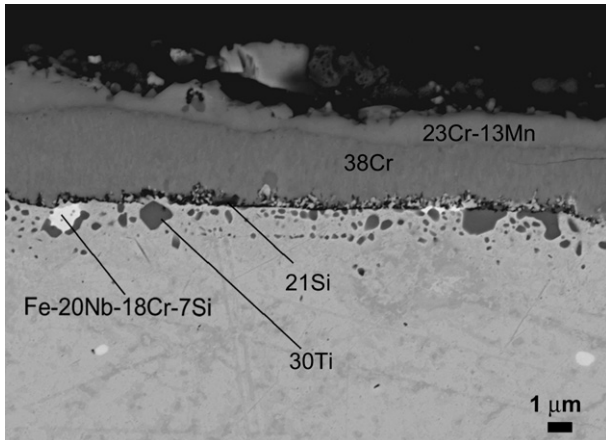


Fig. 4. SEM cross-section at the base metal/scale interface for alloy 441ss exposed for 2000 h at 800 °C is shown above. Note that the values are given in at% and the balance is oxygen (with the exception of Laves phase which has a balance of Fe as shown).

and 33–38 at% Mn (metal basis) with minor amounts of Fe, Nb, Si and Ti. Zone axis diffraction patterns for $[0\bar{1}\bar{1}]$ and $[001]$ grain orientations showed the outer scale to be Cr_2MnO_4 – a cubic structure, with the space group $\text{Fd}-3\text{m}$. Beneath this layer was a much finer grained Cr-rich region containing 96–98 at% Cr and up to 2.4 at% Mn (metal basis, Fig. 7). The small size of the grains and their equiaxed morphology made it difficult to obtain diffraction patterns from single grains. However multi-grain diffraction patterns along with micro-diffraction patterns obtained from zone axis oriented single grains identified this layer as essentially Cr_2O_3 . Beneath the chromia layer was a silicon-rich layer (Fig. 8, this example is from the 430-G alloy). This layer was amorphous as exemplified by the diffuse diffraction ring pattern. The additional details of each of the scales are more complex and will be treated individually.

Alloy 430-G with 500 ppm Si essentially contained a continuous Si-rich layer, nominally ~82 Si, ~13 Cr and ~4.5 Fe (at%, metal basis), at the base of the oxide scale adjacent to the alloy (Fig. 9). It should be noted that the Fe and Cr signals may come from the surrounding oxide and/or base metal due to the limited width of this layer (<100 nm). Alloy 430-F with 240 ppm Si had a similar yet discontinuous Si-rich layer, nominally ~95 Si, ~2 Cr and ~3 Fe (at %, metal basis), residing at the oxide/metal interface and covering about half of this region (Fig. 10). These Si-rich islands measured

about 100–200 nm thick and about 200–400 nm long. These regions were also non-crystalline. It is noteworthy that there is an accumulation of Si in regions adjacent to the islands at the oxide/metal interface (area 'C' ~6 at% Si vs. a background of 0.1 at% Si in the base metal). This seems to indicate an accumulation of Si at the scale/metal interface prior to the formation of the Si-rich phases.

Alloy 430-E with 170 ppm Si had much less distinct Si-rich phase formation (Fig. 11). Some evidence of Si enrichment was found, but not at the levels observed in either of the other two 430 alloys. Several regions were suggestive of being a Si-rich phase. One example measured approximately 50–70 nm (area 'C', Fig. 11). This area, which was found along the scale/metal interface, registered an increased Si to about 1.8 at%. Although by no means conclusive, this observation suggests possible enrichment of the interface as observed in alloy 430-F adjacent to Si-rich phases. In general, Si was preferentially observed to amass at the scale/metal interface and formed phases even at the lowest Si levels in the 430ss alloys.

The oxide sub-scale on the 441ss alloy had several features distinguishing it from the 430ss alloy. One difference concerned internal oxidation of Ti. In 441ss Ti-rich particles were observed at the metal/oxide interface or just below the interface within the metal (Fig. 12). Of course, since the 430ss alloy does not contain Ti, the 430ss alloy samples did not exhibit this feature. The Ti-rich particles contained about 93–94 at% Ti with the balance being mainly Cr (metal basis, Table 2). Detailed analyses of multiple diffraction patterns from multiple Ti-rich particles (Fig. 12) show these particles are most likely a Ti_4O_7 phase with a triclinic crystal structure and P-1 space group.

As reported previously [32] a Si-rich oxide is also found at the scale/metal interface on 441ss. However, it is much more complex in both morphology and chemistry in comparison to the 430ss alloys. Both thick and thin regions of Si were observed on the 441ss alloy (Figs. 13–16). The thin regions measured 10–15 nm in thickness while the thick regions measured 50–200 nm and averaged ~75 nm in thickness. The Si layer in the 430ss alloys also tended to be smooth on both sides. The Si layer is much more irregular in the 441ss alloy, at least in the thicker regions and especially on the side adjacent to the chromia scale. One commonality the layer on the 441ss alloy shares with that on the 430ss alloy is that the Si-rich layer appears to be amorphous. One unique feature of the 441ss alloy is that the Si-rich layer penetrates along the chromia grain boundaries reaching up to 500 nm or so into the chromia grains. This phenomenon was not observed in the 430ss alloys. Many of the Si-rich areas in the 441ss alloy were enriched in Nb compared to the matrix, including some regions well into the chromia scale. One example is an area about 300 nm from the interface (Fig. 14). This island measured about 12 nm across which is much too small for accurate chemical analysis by EDX. However, narrow beam analysis (Region A) showed ~13 Si and ~2 Nb while a broad beam analysis (Region A') showed ~5 Si and ~0.5 Nb (at%, metal basis). It can be inferred that the higher Si and Nb values were coming from the central region and were likely due to the Si-rich phase. Another Si-rich grain which resided about 400 nm from the base metal and measured ~15–25 nm across was interrogated for chemistry along with the four surrounding grains (Fig. 15, Table 3). This central grain contained high Si (~52) and Nb (~1.2) (at%, metal basis, Table 3). It is difficult to get high fidelity chemical analysis from such a small area which is why the surrounding grains were analyzed individually. These were found to be Cr-rich (88–95 at%) or Fe-rich (79–81 at%), Table 3. The Cr-rich grains contained lower levels of Si and Nb than the Si-rich grain (Si: 0.6–4 at% and Nb: 0.3–0.4 at%) which is higher than the base metal (0.4 at% Si and 0.2 at% Nb) but not as high as the Si-rich grain. The Fe-rich grains also contained lower levels of Si and Nb than the Si-rich grain (Si: 0.9–3.2 at % and Nb: 0.5–0.7 at%) which is higher than the base metal but not



Fig. 5. Low magnification TEM image of a FIB cross-section taken from alloy 430-G which is representative of the FIB cross-sections of each of the alloys as well as the general features of the oxide scales.

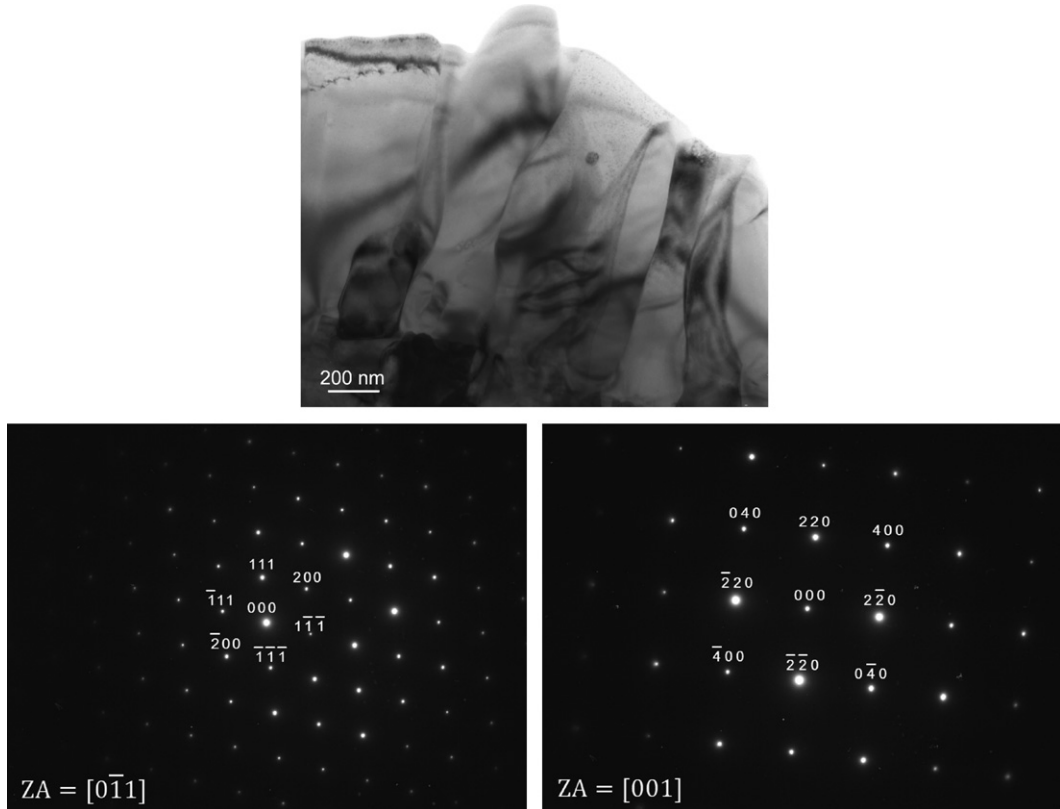


Fig. 6. A TEM image of the typical outer oxide scale found on all the samples is shown above; this example is from alloy 441ss. This scale had a chemistry of 60–65 at% Cr and 33–38 at% Mn (metal basis) and a cubic crystal structure which identified the phase as Cr_2MnO_4 spinel. Representative diffraction patterns are also shown.

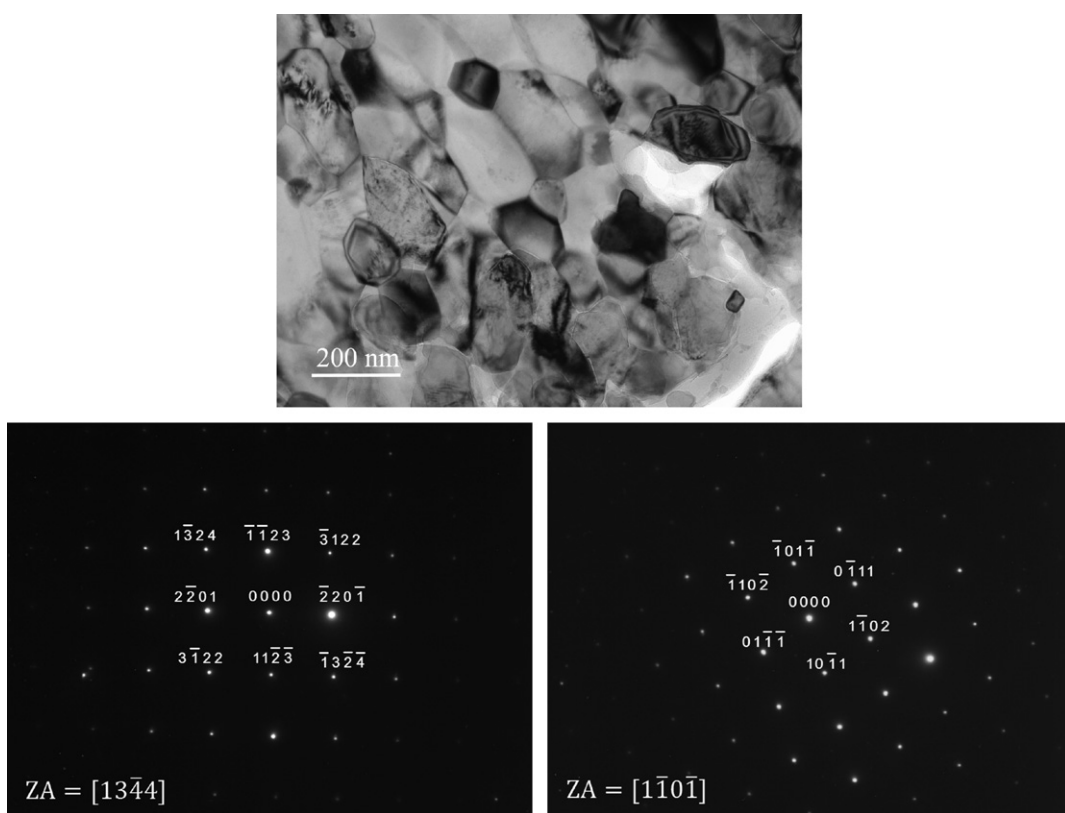


Fig. 7. A TEM image of the typical inner oxide scale found on all the samples is shown above; this example is from alloy 441ss. This scale had a chemistry of essentially pure Cr (metal basis) and a triclinic crystal structure which identified the phase as Cr_2O_3 . Representative diffraction patterns are also shown.

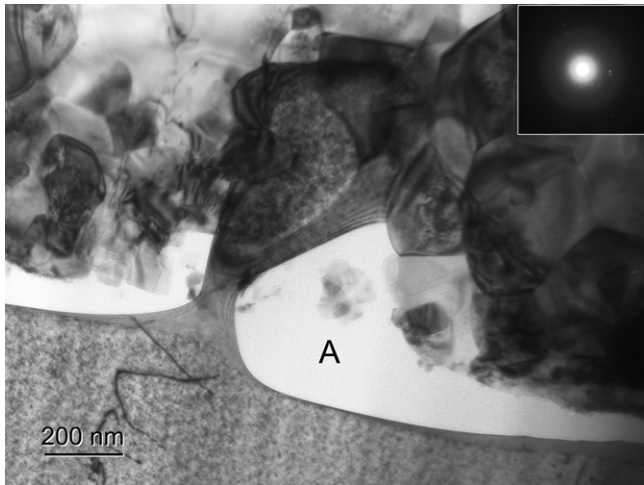


Fig. 8. A TEM image of the typical oxide scale found beneath the Cr_2O_3 (area A) on the 430ss samples is shown above; this example is from alloy 430-G. This scale had a chemistry of 99 at% Si (metal basis) and always exhibited a diffuse diffraction pattern indicating an amorphous structure (inset).

as high as the Si-rich grain. Thus, the high levels of Si and Nb appear to come from the center grain rather than those surrounding it. Another interfacial region is shown in Fig. 16. Here both thick and thin Si-rich areas along with an internal Si-rich phase are presented. There also is evidence of a Si-rich phase along many of the Cr grain boundaries near the interface. The Si in these phases ranged from 34 to 97 while the Nb ranged from 0.5 to 0.7 (at%, metal basis, Table 4). The Cr and Fe ranged from 1 to 14 and 0.8–49.8 (at%, metal basis, Table 4) and is likely mainly from the surrounding material.

4. Discussion

4.1. Oxide scale layers

Based upon the combined SEM and TEM morphological, chemical and structural observations made during the course of

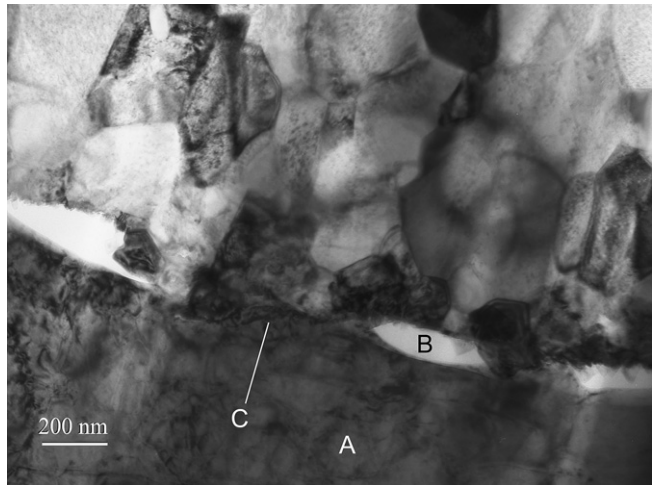


Fig. 10. A TEM image of the typical oxide scale/metal region on the 430-F alloy (240 ppm Si) is shown above. Area 'A' is the matrix which had a typical alloy composition, albeit with a slight Cr and Mn depletion (Fe–14.6Cr–0.1Si–0.1Mn, wt%). Area 'B' was Si-rich with some Cr and Fe, presumably from the surrounding regions (Si–1.0Cr–1.5Fe, at%, metal basis). Area 'C' is an area midway between two Si-rich areas. This area also showed a buildup of Si (Cr–8.3Fe–3.3Mn–10.2Si, at%, metal basis) with the high Cr likely coming from the adjacent chromia scale.

this study, the basic features of the oxide scales on these alloys are as follows: (1) The outer surface is Cr_2MnO_4 spinel having grains elongated in the growth direction and with minor amounts of the remaining transition elements contained in each alloy. (2) Beneath this is a layer of equiaxed grained Cr_2O_3 with very little solubility for the other transition elements with the exception of Mn. (3) Below the Cr_2O_3 there is evidence of an amorphous Si-rich phase which varies in extent. In alloys with 240 ppm or more Si, the Si-rich phase was clearly identified at the base of the Cr_2O_3 . This amorphous Si-rich phase transitioned from discontinuous to nearly continuous when Si content increased from 240 to 500 ppm (430ss alloys). Evidence for this phase in 430ss with 170 ppm Si (alloy 430-E) is less distinct; however, both morphological evidence (Fig. 11) and the analytical results indicates a buildup of Si at the interface

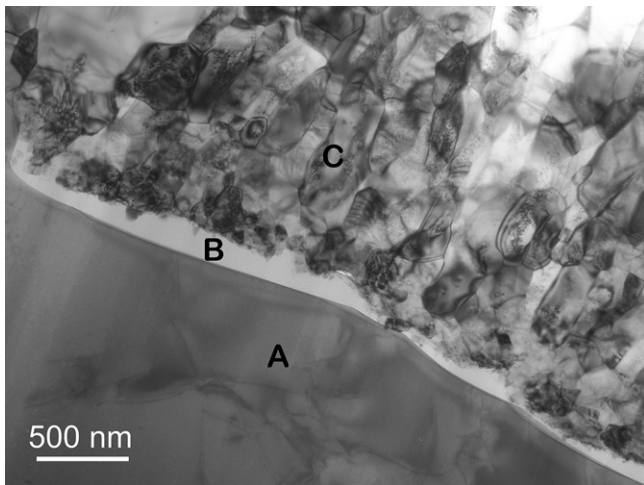


Fig. 9. A TEM image of the typical oxide scale/metal region on the 430-G alloy (500 ppm Si) is shown above. Area 'A' is the matrix which had a typical alloy composition, albeit with a slight Cr depletion (Fe–16.1Cr–0.3Si–0.4Mn, wt%). Area 'B' was Si-rich with some Cr and Fe, presumably from the surrounding regions (Si–7.6Cr–2.5Fe, at%, metal basis). Area 'C' is the chromia scale (Cr–1.0Fe–2.4Mn–0.7Si, at%, metal basis).

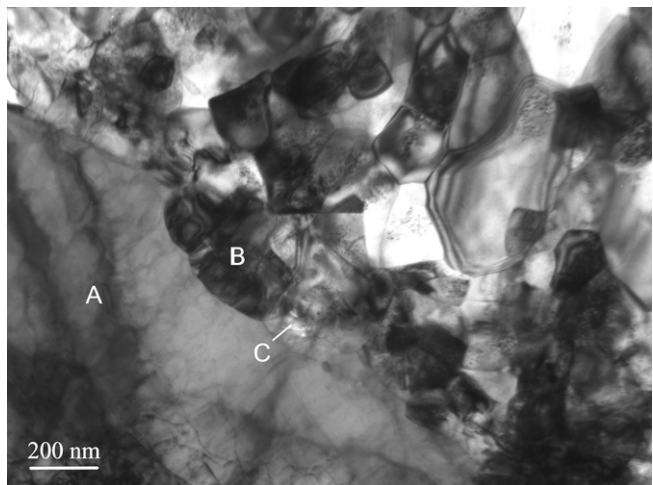


Fig. 11. A TEM image of the typical oxide scale/metal region on the 430-E alloy (170 ppm Si) is shown above. Area 'A' is the matrix which had a typical alloy composition, albeit with a slight Cr depletion (Fe–14.4Cr–0.2Si–0.3Mn, wt%). Area 'B' was a chromia grain adjacent to the base alloy (Cr–1.9Fe–5.3Mn–0.8Si, at%, metal basis). Area 'C' is at the chromia/alloy interface which showed a buildup of Si (Cr–2.6Fe–7.6Mn–1.8Si, at%, metal basis).

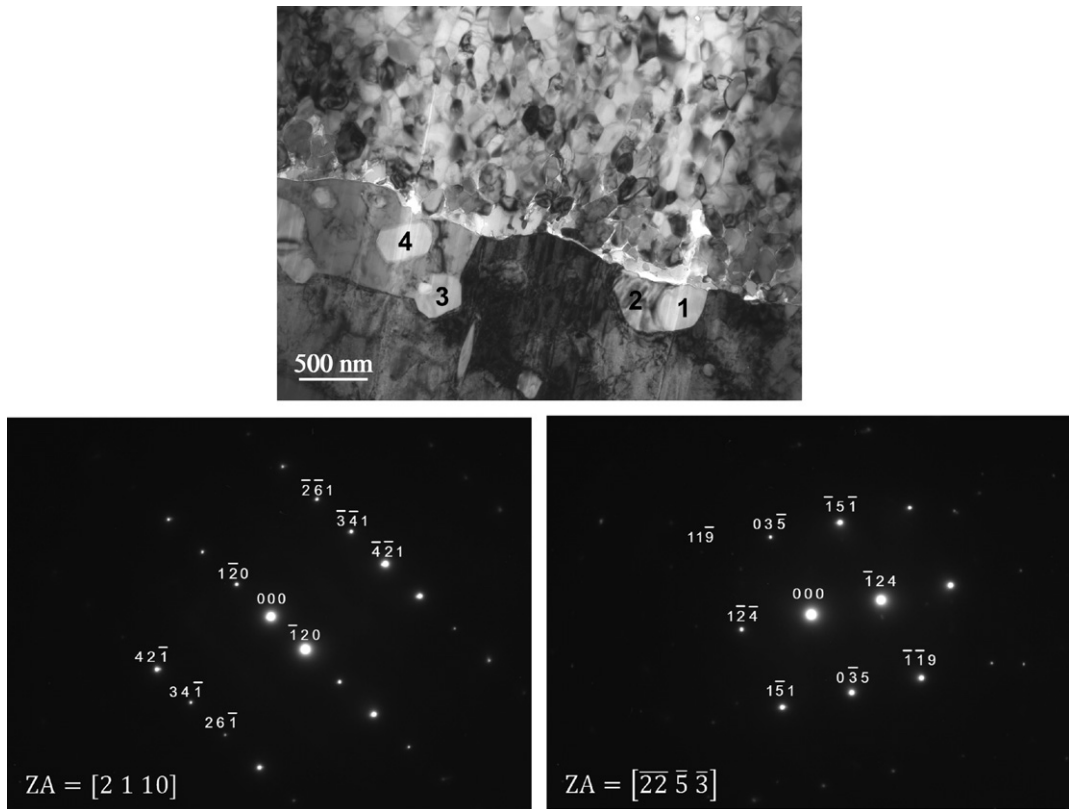


Fig. 12. A TEM image of the typical oxide scale/metal region in alloy 441ss is shown above. The indicated particles were found to be Ti-rich (Table 2). These particles were identified to be a Ti_4O_7 phase with a triclinic crystal structure and P-1 space group.

and suggests that this alloy may be in the early stages of Si-rich phase formation. SEM and TEM results clearly show a buildup of Si at the Cr_2O_3 /metal interface of the 430 alloys even with Si levels as low as 170 ppm. These results suggest that in order to avoid the Si-rich layer after long exposure, such as during the 40,000 h expected life cycle for an SOFC interconnect, the Si level in the alloy needs to be below 170 ppm and perhaps as close to zero percent as possible. Reducing Si to such low levels would be very difficult to achieve during production without strict control of input materials and processing conditions.

The major features of the oxide scale, i.e., the Cr/Mn-rich outer and Cr-rich inner scales, have been well reported on in the literature [22,25,29,34,36–38]. Present understanding is that initially Cr_2O_3 forms on the surface of the alloy after exposure times as short as 15 min [39], perhaps sooner. With additional exposure (or quick diffusion pathways such as alloy grain boundaries) Mn from the alloy diffuses to the top of the oxide scale and combines with the Cr to form a Cr/Mn-rich scale on the outer surface. The Mn appears at the top of the scale because of its high affinity for oxygen (comparable ΔG for oxidation compared to Cr, Table 5). Additionally, Mn has a high diffusion rate within the base metal matrix

(about twice that of Cr at 800 °C), providing a constant supply of Mn to the metal/scale interface (Table 6). Thirdly, there is sufficient solubility (measurements as high as 2.4 at% were made) for Mn in the Cr_2O_3 scale that forms initially, providing a supply of Mn to the surface. And finally, the higher diffusivity of Mn^{2+} cations through the underlying oxide ensures its preferential delivery to the surface [40]. From Table 6 it is apparent that Mn, Si and Ti have comparable diffusivities within their respective alloy matrices while that of Nb is 2–3 times greater. Thus, these elements are able to diffuse within

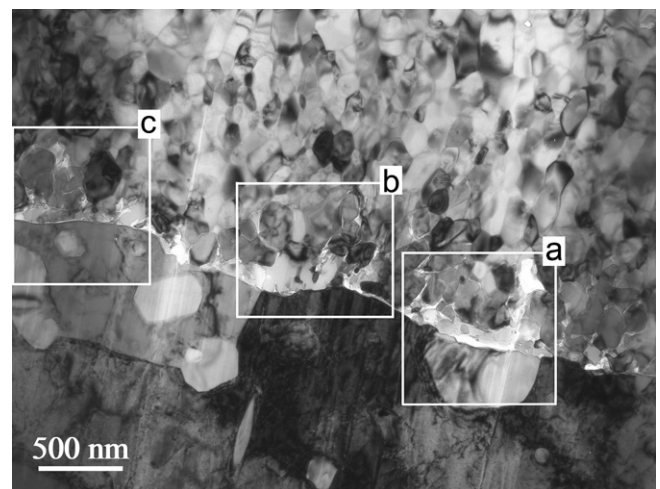


Fig. 13. A TEM image of the typical oxide scale/metal region on the 441 alloy is shown above. The boxed areas are further described in subsequent figures.

Table 2

Compositions of the indicated particles in Fig. 12 obtained by TEM based EDX analysis. Values in the table are given in atomic percent (at%) on a metal only basis.

| Particle | Si | Nb | Ti | Cr | Mn | Fe |
|----------|-----|-----|------|-----|-----|-----|
| 1 | 1.0 | 0.4 | 93.7 | 4.1 | 0.1 | 0.6 |
| 2 | 1.1 | 0.3 | 93.8 | 4.0 | 0.2 | 0.6 |
| 3 | 0.9 | 0.2 | 94.0 | 4.1 | 0.1 | 0.7 |
| 4 | 1.4 | 0.3 | 92.6 | 4.8 | 0.1 | 0.8 |

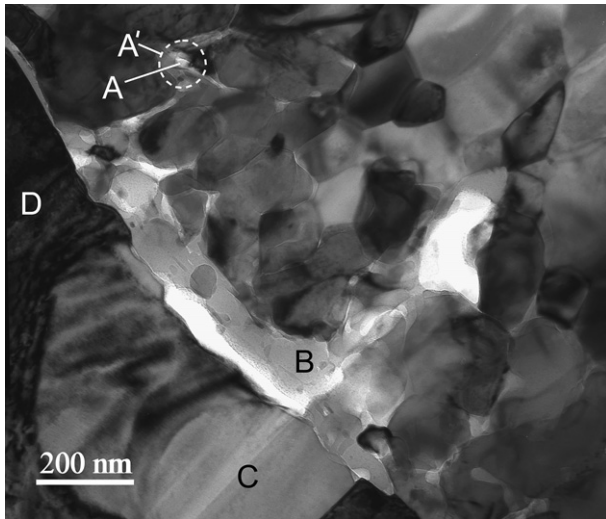


Fig. 14. A higher magnification TEM image of boxed area 'a' from Fig. 13 is shown above. A broad beam analysis of area 'A' gave 4.6 Si and 0.5 Nb while a narrow beam located at area 'A' returned 12.7 Si and 1.9 Nb (at%, metal basis) indicating a buildup of Si and Nb in that area.

the matrix, presumably under the influence of the compositional gradient set up by their initial oxidation. However, the Si contained in both 430ss and 441ss as well as the Nb and Ti contained in the 441ss appear to have much lower solubility in the Cr_2O_3 scale based on analysis of the scales. Their respective cations also have lower diffusivities in the oxide [40]. Thus, these elements are not able to diffuse through the scale to the scale/air surface, and therefore, reside where they originally oxidize. Interestingly, Ti has the highest ΔG for oxidation and thus forms an oxide furthest into the alloy, even below the subscale layer which would have the lowest oxygen activity. It is the lower oxygen activity that causes the sub oxide, Ti_4O_7 , to form rather than the more conventional TiO_2 .

4.2. Si-rich oxides: 430ss vs. 441ss

There are several significant differences between the Si-rich scales found on the 430ss and 441ss alloys. Morphologically, the

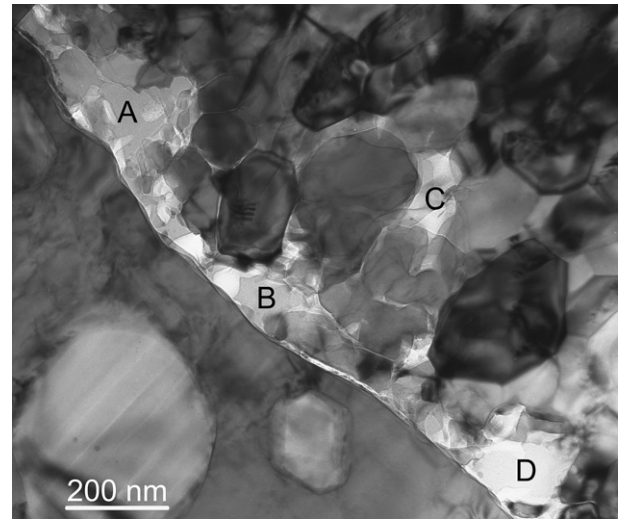


Fig. 16. A higher magnification TEM image of boxed area 'c' from Fig. 13 is shown above. A narrow beam analysis of the indicated areas showed that they were high in Si and Nb (Table 4).

Table 3

The regions in the table below are the Si-rich areas and surrounding grains as identified in Fig. 15 (values in at% on a metal only basis).

| Region | Si | Nb | Ti | Cr | Mn | Fe |
|--------|------|-----|-----|------|-----|------|
| A | 52.1 | 1.2 | 0.2 | 13.5 | 0.1 | 32.9 |
| B | 3.2 | 0.7 | 0.1 | 17.0 | 0.0 | 79.0 |
| C | 0.6 | 0.3 | 1.9 | 95.2 | 0.2 | 1.8 |
| D | 0.9 | 0.5 | 0.2 | 17.4 | 0.0 | 81.0 |
| E | 4.0 | 0.4 | 1.5 | 88.4 | 0.0 | 5.7 |
| F | 98.2 | 0.4 | 0.2 | 0.4 | 0.2 | 0.6 |
| G | 0.8 | 0.1 | 0.7 | 17.4 | 0.3 | 80.7 |

Si scale on the 430ss alloys was smooth and planar, and was only found at the Cr_2O_3 scale/metal interface. Some variation in thickness was observed which was probably due to multiple nucleation events at the interface followed by lateral growth as observed on the 430-F alloy (Fig. 10). In stark contrast to this was the Si scale observed on the 441ss alloy. In this case the presence of Ti and Nb reduces the Si diffusivity in the matrix by less than 10% (Table 6). The Si-rich scale on the 441ss alloy was irregular in thickness, ranging from 10 to 15 nm in thin areas and 50–200 nm (~ 75 nm average) in thick areas even though this alloy had nearly 10× the Si compared to the 430ss alloys (Figs. 13–16). Another significant morphological distinction was that the Si-rich scale was found intergranularly within the Cr_2O_3 scale both as films and islands. The fact that it was observed as film implies that its interfacial energy with Cr_2O_3 grains is perhaps lower than the $\text{Cr}_2\text{O}_3/\text{Cr}_2\text{O}_3$ interfacial (grain boundary) energy. It is noteworthy that while the Si-rich phase in the 430ss alloys appeared to be primarily Si (the Cr and Fe detected could be attributable to the surrounding phases), significant Nb was detected in many of the Si-rich regions in 441ss and range from 1 to 3 at%. This level is quite significant and cannot be attributed to matrix effects because of the low matrix level of Nb.

Table 4

The regions in the table below are the Si-rich areas as identified in Fig. 16 (values in at% on a metal only basis).

| Region | Si | Nb | Ti | Cr | Mn | Fe |
|--------|------|-----|-----|------|-----|------|
| A | 81.0 | 0.6 | 0.6 | 3.8 | 0.1 | 13.9 |
| B | 34.4 | 0.7 | 0.8 | 14.0 | 0.3 | 49.8 |
| C | 84.1 | 0.7 | 0.3 | 11.7 | 0.1 | 3.1 |
| D | 97.3 | 0.5 | 0.3 | 1.0 | 0.1 | 0.8 |

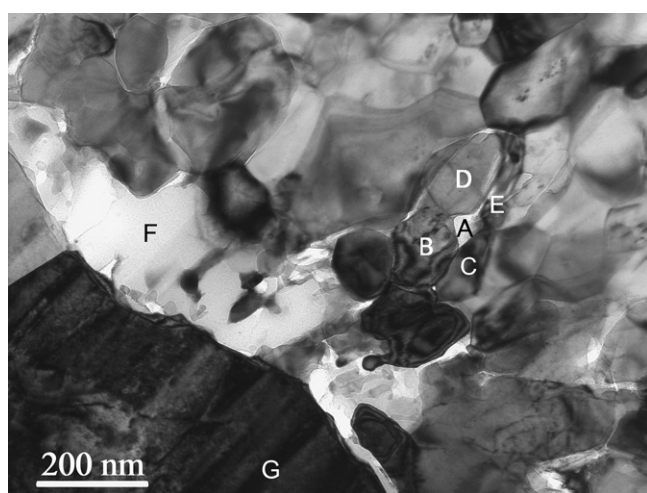


Fig. 15. A higher magnification TEM image of boxed area 'b' from Fig. 13 is shown above. The chemistries of the indicated analysis points A–E are found in Table 3. Area F is a broad region of Si-rich sub-scale. Area G is the 441ss base metal.

Table 5

Driving force for the formation of the various oxides is given in the table below. These driving forces were calculated using Thermo-Calc, using the TCFE6, SSUB4 and TCOx4 databases with the temperature set at 800 °C and the alloy chemistry set to 441ss.

| Oxide phase | $-\Delta G$ (kJ mol $^{-1}$) |
|---------------------------------------|-------------------------------|
| TiO ₂ | 217 |
| Ti ₄ O ₇ | 214 |
| Ti ₃ O ₅ | 210 |
| Ti ₂ O ₃ | 207 |
| MnTiO ₃ | 189 |
| Nb ₂ O ₅ | 185 |
| SiO ₂ | 180 |
| NbO ₂ | 178 |
| Mn ₂ TiO ₄ | 175 |
| TiO | 174 |
| FeTiO ₃ | 173 |
| MnSiO ₃ | 164 |
| Cr ₂ O ₃ | 164 |
| Cr ₂ MnO ₄ | 161 |
| Mn ₂ SiO ₄ | 161 |
| Mn ₂ O ₃ | 157 |
| Fe ₂ TiO ₄ | 151 |
| Cr ₂ FeO ₄ | 150 |
| FeSiO ₃ | 137 |
| (Fe,Mn) ₂ SiO ₄ | 134 |
| MnO | 134 |
| NbO | 132 |
| Mn ₃ O ₄ | 128 |
| CrO ₂ | 122 |
| Fe ₂ MnO ₄ | 115 |
| Cr ₅ O ₁₂ | 106 |
| Fe ₃ O ₄ | 105 |
| Fe ₂ O ₃ | 104 |
| FeO | 97 |
| Cr ₈ O ₂₁ | 93 |
| MnO ₂ | 93 |
| CrO ₃ | 71 |

Furthermore, the Si-rich regions containing Nb were found far from Laves phase particles which contain appreciable Nb. It may be that the Nb acts as a charge compensator within the glassy Si-O matrix since it can exist as either Nb³⁺ or Nb⁵⁺ ions while the Si is limited to Si⁴⁺. This would help to explain the apparent lower interfacial energy with Cr₂O₃ as compared to Cr₂O₃/Cr₂O₃ grain boundaries since charge defects at Nb-doped-Si-oxide/Cr₂O₃ boundaries could be more easily accommodated compared to Cr₂O₃/Cr₂O₃ grain boundaries. Additionally, doping with Nb could help the Si-rich layer become conductive, especially under SOFC operating

Table 6

Chemical diffusivities of various elements are given in the table below for a range of chemistries in both 441ss and 430ss (nominal chemistries). The diffusivities in this table were calculated using DICTRA and the TCFE6 and MOB2 databases, with the temperature set at 800 °C and the alloy chemistry set to 441ss or 430ss.

| Diffusing species | Weight percent | Chemical diffusivity in 441ss \bar{D} (m s $^{-2}$) | Chemical diffusivity in 430ss \bar{D} (m s $^{-2}$) |
|-------------------|----------------|--|--|
| Cr | 0.0 | 3.30E-16 | 3.30E-16 |
| | 17.0 | 6.20E-16 | 6.40E-16 |
| | 18.0 | 6.10E-16 | 6.30E-16 |
| Mn | 0.0 | 1.20E-15 | 1.20E-15 |
| | 0.3 | 1.30E-15 | 1.30E-15 |
| | 1 | 1.30E-15 | 1.30E-15 |
| Nb | 0.0 | 3.80E-15 | |
| | 0.5 | 3.60E-15 | |
| | 1.0 | 3.40E-15 | |
| Si | 0.0 | 1.20E-15 | 1.10E-15 |
| | 0.3 | 1.40E-15 | 1.30E-15 |
| | 1.0 | 2.00E-15 | 1.90E-15 |
| Ti | 0.0 | 1.00E-15 | |
| | 0.2 | 1.00E-15 | |
| | 1.0 | 1.10E-15 | |

conditions. Thus, Nb may help reduce the area specific resistance (ASR) of the Si-rich phase as the Nb can act as an electron donor or receptor. This may help explain the low, long term, ASR results on 441ss reported by some researchers [25].

5. Summary

It is generally accepted that silica subscale formation greatly increases the ASR and reduces the performance of a SOFC, and should be avoided. Therefore, the maximum allowable Si level in ferritic stainless steel in order to avoid the formation of Si-rich subscales should be zero or as near to zero as practical based on this present investigation. However, there are many significant differences between the Si-rich subscale that forms on the 441ss and the 430ss alloys (and perhaps other ferritic stainless steels as well). The Si-rich subscale that forms on the 441ss alloy is very irregular in thickness. This provides for low resistance pathways during SOFC operation and may help explain the low long term ASR results reported by some researchers. Additionally, the Si-rich scale was found intergranularly within the Cr₂O₃ scale both as film and islands, suggesting that the interfacial energy between this phase and the Cr₂O₃ scale is lower than the Cr₂O₃/Cr₂O₃ interfacial energy. Furthermore, the Si-rich subscale that forms on the 441ss appears to be doped with Nb, which may help to reduce the ASR of the Si-rich phase since the Nb can act as an electron donor or receptor. These unique characteristics of the Si-rich scale that forms on 441ss contribute to the low electrical resistance observed on this alloy.

Disclaimer

"This report was prepared as an account of work sponsored by an agency of the United States Government. Neither the United States Government nor any agency thereof, nor any of their employees, makes any warranty, express or implied, or assumes any legal liability or responsibility for the accuracy, completeness, or usefulness of any information, apparatus, product, or process disclosed, or represents that its use would not infringe privately owned rights. Reference herein to any specific commercial product, process, or service by trade name, trademark, manufacturer, or otherwise does not necessarily constitute or imply its endorsement, recommendation, or favoring by the United States Government or any agency thereof. The views and opinions of authors expressed herein do not necessarily state or reflect those of the United States Government or any agency thereof."

Acknowledgments

The authors wish to acknowledge the contributions of our colleagues at NETL-Albany: Ed Argetsinger, Paul Danielson, Dave Smith, Richard Chinn, Keith Collins, and Marisa Arnold. The authors also wish to acknowledge the work of Kurt A. Langworthy of the University of Oregon's CAMCOR facility in preparing the FIB TEM samples. Finally, the authors wish to acknowledge the helpful suggestions of Jeffery Hawk and David Maurice both of NETL.

References

- [1] Fuel Cell Handbook, under contract number DE-AM26-99FT40575 with US Dept of Energy, Office of Fossil Energy, National Energy Technology Laboratory, seventh ed., EG&G Technical Services, 2004 (Chapter 1).
- [2] Mark C. Williams, Joseph P. Strakey, Wayne A. Surdoval, *J. Power Sources* 143 (2005) 101–196.
- [3] Mark C. Williams, Joseph P. Strakey, Wayne A. Surdoval, Lane C. Wilson, *Solid State Ionics* 177 (2006) 2039–2044.
- [4] Mark C. Williams, Joseph P. Strakey, Wayne A. Surdoval, *J. Power Sources* 159 (2006) 1241–1247.
- [5] S. de Souza, S.J. Visco, L.C. De Jonghe, *Solid State Ionics* 98 (1997) 57.

- [6] H. Ishihara, H. Matsuda, Y. Takita, *J. Am. Chem. Soc.* 116 (1994) 3801.
- [7] M. Feng, J.B. Goodenough, *Eur. J. Solid State Inorg. Chem.* T31 (1994) 663.
- [8] P. Huang, A. Petric, *J. Electrochem. Soc.* 143 (5) (1996) 1644.
- [9] K.Q. Huang, R. Tichy, J.B. Goodenough, *J. Am. Ceram. Soc.* 81 (1998) 2565.
- [10] W.Z. Zhu, S.C. Deevi, *Mat. Res. Bull.* 38 (2003) 957–972.
- [11] S.P. Simner, M.D. Anderson, G.-G. Xia, Z. Yang, L.R. Pederson, J.W. Stevenson, *J. Electrochem. Soc.* 152 (4) (2005) A740.
- [12] M.C. Tucker, H. Kurokawa, C.P. Jacobson, L.C. De Jonghe, S.J. Visco, *J. Power Sources* 160 (2006) 130.
- [13] M. Kumpelt, T. Kaun, T.A. Cruse, M. Hash, SECA Annual Workshop, May 11–13, 2004, available at: <http://www.seca.doe.gov>.
- [14] S.P.S. Badwal, R. Deller, K. Fogar, Y. Ramprakash, J.P. Zhang, *Solid State Ionics* 99 (1997) 297.
- [15] Y. Matsuzaki, I. Yasuda, *Solid State Ionics* 132 (2000) 271.
- [16] S.P. Jiang, J.P. Zhand, X.G. Zheng, *J. Eur. Ceram. Soc.* 22 (2002) 361.
- [17] Z. Yang, G. Xia, P. Singh, J.W. Stevenson, *J. Power Sources* 155 (2006) 246.
- [18] X. Chen, P.Y. Hou, C.P. Jacobson, S.J. Visco, L.C. De Jonghe, *Solid State Ionics* 176 (2005) 425–433.
- [19] Z. Yang, G. Xia, G. Maupin, J. Stevenson, *Surf. Coat. Technol.* 201 (2006) 4476–4483.
- [20] Z. Yang, G. Xia, X. Li, J. Stevenson, *Int. J. Hydrogen Energy* 32 (2007) 3648–3654.
- [21] Junwei Wu, Christopher D. Johnson, Randall S. Gemmen, Xingbo Liu, *J. Power Sources* 189 (2009) 1106.
- [22] D.E. Alman, P.D. Jablonski, *Int. J. Hydrogen Energy* 32 (2007) 793.
- [23] D. Dulieu, J. Cotton, H. Greiner, K. Honegger, A. Scholten, T. Seguelong, in: P. Stevens (Ed.), *Proceedings of Third European SOFC Forum, European Solid Oxide Fuel Cell Forum, Switzerland* (1998), p. 447.
- [24] S. Chandra-Ambhorn, Y. Wouters, L. Antoni, F. Toscan, A. Galerie, *J. Power Sources* 171 (2007) 688.
- [25] Z. Yang, G. Xia, C. Wang, Z. Nie, J. Templeton, J. Stevenson, P. Singh, *J. Power Sources* 183 (2008) 660–667.
- [26] Metals HandbookProperties and Selection: Irons, Steels, and High-performance Alloys, tenth ed., vol. V1, ASM International, Materials Park, OH, 1990, p. 847.
- [27] <http://www.alleghenyludlum.com/ludlum/Documents/441.pdf>.
- [28] T.B. Massalski (Ed.), *Fe–ni Phase Diagram in Binary Alloy Phase Diagrams*, second ed., ASM International, Materials Park, OH, 1992. p. 1732.
- [29] J. Froitzheim, G.H. Meier, L. Niewolak, P.J. Ennis, H. Hattendorf, L. Singheiser, W.J. Quadakkers, *J. Power Sources* 178 (2008) 163–173.
- [30] N. Fujita, K. Ohmura, A. Yamamoto, *Mat. Sci. Eng. A* 359 (2003) 272–281.
- [31] T.F. de Andrade, A.M. Kliauga, R.L. Plaut, A.F. Padilha, *Mater. Char.* 59 (2008) 503–507.
- [32] P.D. Jablonski, C.J. Cowen, J.S. Sears, *J. Power Sources* 195 (2010) 813–820.
- [33] G.M. Sim, J.C. Ahn, S.C. Hong, K.J. Lee, L.S. Lee, *Mat. Sci. Eng. A* 396 (2005) 159–165.
- [34] T. Horita, H. Kishimoto, K. Yamaji, Y. Xiong, N. Sakai, M.E. Brito, H. Yakokawa, *J. Power Sources* 176 (2008) 54–61.
- [35] Jablonski, Cowen, *Met Trans. 40B* (2009) 182.
- [36] J. Rufner, P. Gannon, P. White, M. Deibert, S. Teintze, R. Smith, H. Chen, *Int. J. Hydrogen Energy* 33 (2008) 1392–1398.
- [37] S. Geng, J. Zhu, *J. Power Sources* 160 (2006) 1009–1016.
- [38] S.J. Geng, J.H. Zhu, Z.G. Lu, *Scr. Mater.* 55 (2006) 239–242.
- [39] J. Zhu, L.M. Ferdanand Diaz, G.R. Holcomb, P.D. Jablonski, C.J. Cowen, D.E. Laughlin, D. Alman, S. Sridhar, *J. Electrochem. Soc.* 157 (5) (2010) B655–B664.
- [40] M.G.C. Cox, B. McEnaney, V.D. Scott, *Philos. Mag.* 26 (4) (1972) 839–851.